PHANGS-JWST First Results: Measuring Polycyclic Aromatic Hydrocarbon Properties across the Multiphase Interstellar Medium

Jérémy Chastenet, Jessica Sutter, Karin Sandstrom, Francesco Belfiore, Oleg V. Egorov, Kirsten L. Larson, Adam K. Leroy, Daizhong Liu, Erik Rosolowsky, David A. Thilker, et al.

The Astrophysical Journal Letters, 944:L12 (10pp), 2023 February 20 https://doi.org/10.3847/2041-8213/acac94

PHANGS–JWST First Results: Measuring Polycyclic Aromatic Hydrocarbon Properties across the Multiphase Interstellar Medium

Jérémy Chastenet[1], Jessica Sutter[2], Karin Sandstrom[2], Francesco Belfiore[3], Oleg V. Egorov[4], Kirsten L. Larson[5], Adam K. Leroy[6,7], Daizhong Liu[8], Erik Rosolowsky[9], David A. Thilker[10], Elizabeth J. Watkins[4], Thomas G. Williams[11,12], Ashley. T. Barnes[13], F. Bigiel[13], Médéric Boquien[14], Mélanie Chevance[15,16], Daniel A. Dale[17], J. M. Diederik Kruijssen[16], Eric Emsellem[18,19], Kathryn Grasha[20], Brent Groves[21], Hamid Hassani[9], Annie Hughes[22], Kathryn Kreckel[4], Sharon E. Meidt[1], Hsi-An Pan[23], Miguel Querejeta[24], Eva Schinnerer[12], and Cory M. Whitcomb[25]

[1] Sterrenkundig Observatorium, Ghent University, Krijgslaan 281-S9, B-9000 Gent, Belgium; jeremy.chastenet@ugent.be
[2] Center for Astrophysics and Space Sciences, Department of Physics, University of California, San Diego 9500 Gilman Drive, La Jolla, CA 92093, USA
[3] INAF—Arcetri Astrophysical Observatory, Largo E. Fermi 5, I-50125, Florence, Italy
[4] Astronomisches Rechen-Institut, Zentrum für Astronomie der Universität Heidelberg, Mönchhofstraße 12-14, D-69120 Heidelberg, Germany
[5] AURA for the European Space Agency (ESA), Space Telescope Science Institute, 3700 San Martin Drive, Baltimore, MD 21218, USA
[6] Department of Astronomy, The Ohio State University, 140 West 18th Avenue, Columbus, Ohio 43210, USA
[7] Center for Cosmology and Astroparticle Physics, 191 West Woodruff Avenue, Columbus, OH 43210, USA
[8] Max-Planck-Institut für Extraterrestrische Physik (MPE), Giessenbachstr. 1, D-85748 Garching, Germany
[9] Department of Physics, University of Alberta, Edmonton, Alberta, T6G 2E1, Canada
[10] Department of Physics and Astronomy, The Johns Hopkins University, Baltimore, MD 21218, USA
[11] Sub-department of Astrophysics, Department of Physics, University of Oxford, Keble Road, Oxford OX1 3RH, UK
[12] Max-Planck-Institut für Astronomie, Königstuhl 17, D-69117, Heidelberg, Germany
[13] Argelander-Institut für Astronomie, Universität Bonn, Auf dem Hügel 71, D-53121, Bonn, Germany
[14] Centro de Astronomía (CITEVA), Universidad de Antofagasta, Avenida Angamos 601, Antofagasta, Chile
[15] Institut für Theoretische Astrophysik, Zentrum für Astronomie der Universität Heidelberg, Albert-Ueberle-Strasse 2, D-69120 Heidelberg, Germany
[16] Cosmic Origins Of Life (COOL) Research DAO, coolresearch.io
[17] Department of Physics and Astronomy, University of Wyoming, Laramie, WY 82071, USA
[18] European Southern Observatory, Karl-Schwarzschild-Straße 2, D-85748 Garching, Germany
[19] Univ Lyon, Univ Lyon1, ENS de Lyon, CNRS, Centre de Recherche Astrophysique de Lyon UMR5574, F-69230 Saint-Genis-Laval France
[20] Research School of Astronomy and Astrophysics, Australian National University, Canberra, ACT 2611, Australia
[21] International Centre for Radio Astronomy Research, University of Western Australia, 7 Fairway, Crawley, 6009 WA, Australia
[22] IRAP, Université de Toulouse, CNRS, CNES, UPS, (Toulouse), France
[23] Department of Physics, Tamkang University, No. 151, Yingzhuan Road, Tamsui District, New Taipei City 251301, Taiwan
[24] Observatorio Astronómico Nacional (IGN), C/Alfonso XII, 3, E-28014 Madrid, Spain
[25] Ritter Astrophysical Research Center, University of Toledo, Toledo, OH 43606, USA
Received 2022 October 21; revised 2022 December 16; accepted 2022 December 17; published 2023 February 16

Abstract

Ratios of polycyclic aromatic hydrocarbon (PAH) vibrational bands are a promising tool for measuring the properties of the PAH population and their effect on star formation. The photometric bands of the MIRI and NIRCam instruments on JWST provide the opportunity to measure PAH emission features across entire galaxy disks at unprecedented resolution and sensitivity. Here we present the first results of this analysis in a sample of three nearby galaxies: NGC 628, NGC 1365, and NGC 7496. Based on the variations observed in the 3.3, 7.7, and 11.3 μm features, we infer changes to the average PAH size and ionization state across the different galaxy environments. High values of F335M$_{\rm PAH}$/F1130W and low values of F1130W/F770W are measured in H II regions in all three galaxies. This suggests that these regions are populated by hotter PAHs, and/or that the PAH ionization fraction is larger. We see additional evidence of heating and/or changes in PAH size in regions with higher molecular gas content as well as increased ionization in regions with higher Hα intensity.

Unified Astronomy Thesaurus concepts: Dust physics (2229); Interstellar dust (836); Polycyclic aromatic hydrocarbons (1280)

1. Introduction

The mid-infrared (mid-IR) emission features at 3.3, 6.2, 7.7, 8.6, 11.3, 12.6, and 17 μm first seen in Milky Way star-forming regions (Gillett et al. 1973; Merrill et al. 1975) and later observed in the spectrum of star-forming galaxies (e.g., Smith et al. 2007) have been attributed to the vibrational modes of large carbonaceous molecules (Allamandola et al. 1989; Draine & Li 2001; Tielens 2008a), referred to as polycyclic aromatic hydrocarbons (PAHs; Leger & Puget 1984; Allamandola et al. 1985), or in some models, to the same modes of surface H atoms in the aromatic mantle of dust grains (Jones et al. 2017). PAHs are important in a variety of processes in the interstellar medium (ISM), including photoelectric heating of neutral gas (Bakes & Tielens 1994; Wolfire et al. 1995; Weingartner & Draine 2001) and the formation of H_2 (Le Page et al. 2009; Le Bourlot et al. 2012).

The characteristics of these molecules, including their size, charge, hydrogenation, and structure, determine the efficiency of these processes (e.g., the charge state of PAHs determines

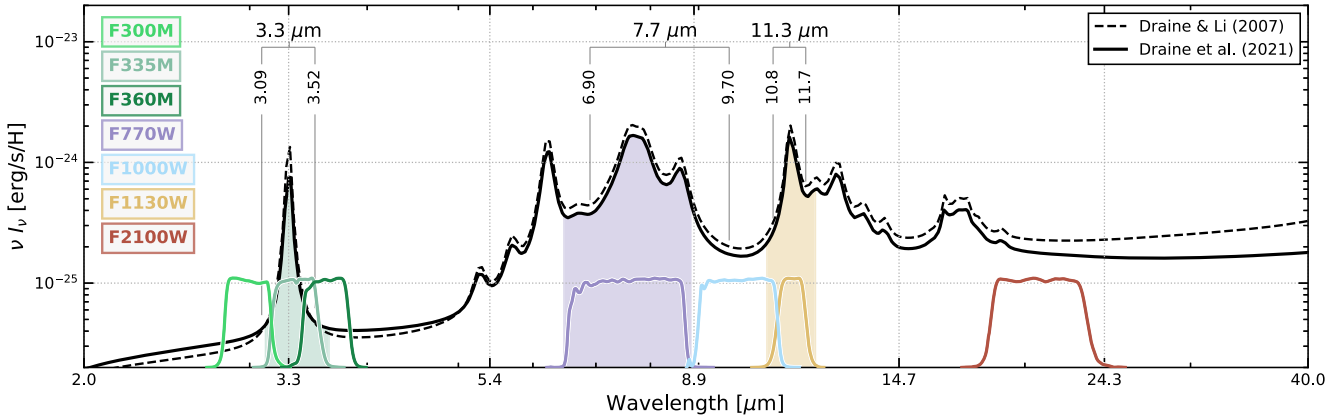

Figure 1. Visual representation of some of the NIRCam, and the MIRI filters, with their normalized transmission curves, in color, and associated integrated area for the three main filters used in this study. The vertical lines and the shaded regions mark the wavelength cuts for the clip points defined in Draine et al. (2021) that they used to integrate the feature luminosities. The associated complexes are labels on top. The black solid and dashed lines are representative mid-IR spectra from Draine & Li (2007), $U = 1.0$, $b_C = 0.0$, and Draine et al. (2021) "mMMP" with $U = 1.0$, "st" ionization and "std" size, for comparison.

the efficiency of the photoelectric effect; Tielens 2008a), and set the relative strength of the various mid-IR vibrational bands (Maragkoudakis et al. 2020). Intensive laboratory and theoretical work continues to identify the contributing species to each of these emission features or complexes of features (e.g., Boersma et al. 2014; Bauschlicher et al. 2018; Mattioda et al. 2020; Kerkeni et al. 2022). Observations of PAH band ratios can use this information to infer properties like average size and ionization by modeling the distribution of PAHs that contribute to the observed emission (e.g., Draine et al. 2021; Rigopoulou et al. 2021; Kerkeni et al. 2022; Maragkoudakis et al. 2022).

Some of these features are now generally agreed to be produced by specific types of PAHs. For instance, the 3.3 μm feature is characteristic of small, neutral PAHs, while the 7.7 μm complex traces vibrational bands produced by larger, positively charged ions, and the 11.3 μm is representative of populations of grains that are both larger and neutral (e.g., Galliano et al. 2008; Boersma et al. 2016, 2018; Maragkoudakis et al. 2020; Draine et al. 2021; Rigopoulou et al. 2021; Maragkoudakis et al. 2022). The ratios of these bands can therefore constrain quantities such as the relative amounts of small to large PAHs (in terms of number of carbon atoms) and the fraction of ionized to neutral PAHs.

Determining how these ratios vary across a galaxy can also provide important context for how the PAHs are influencing the surrounding ISM. For example, higher fractions of ionized PAHs could lead to a decrease in the photoelectric heating efficiency, as highly charged grains will have higher ionization potentials (Tielens 2008b). This has been observed in variations in the relative strength of far-infrared cooling lines compared to total infrared luminosity as a function of PAH feature ratios, suggesting the properties of the PAHs influence the balance of ISM heating and cooling (Croxall et al. 2012; McKinney et al. 2021; Sutter & Fadda 2022). As both a source and sink for free electrons, PAHs also play a large role in setting the ionization balance (Bakes & Tielens 1994; Li 2020). Understanding the properties of the PAHs as traced by band ratios will therefore help establish how these important molecules influence ISM conditions.

The James Webb Space Telescope (JWST) opens a new era in PAH studies by simultaneously offering a diverse suite of filters covering many key PAH features, and offering unprecedented resolution in the mid-IR.

While previously restricted to Local Group galaxies (see, e.g., Sandstrom et al. 2012), it is now possible to directly probe these ratios across the disks of nearby galaxies, at small physical scales (tens of parsecs), with JWST. With the NIRCam instrument (Rieke et al. 2005) covering the 3.3 μm feature, and the MIRI instrument (Rieke et al. 2015) covering the 7.7 and 11.3 μm complexes, we can investigate the properties of PAHs across the extent of $D \lesssim 20$ Mpc galaxies at $\sim$10–50 pc resolution. The sensitivity of JWST further enables measurements of the PAH properties in multiple phases of the ISM (e.g., diffuse atomic gas, molecular clouds without massive star-forming regions, molecular clouds with associated H II regions, diffuse ionized gas), not just the bright star-forming complexes that were visible to Spitzer Infrared Spectrograph (IRS).

In this Letter we deploy this new capability to measure the resolved variations in PAH band ratios in three of the first targets of the PHANGS–JWST survey (Lee et al. 2023). We make maps of the F335M$_{\rm PAH}$/F770W, F335M$_{\rm PAH}$/F1130W, and F1130W/F770W over wide areas to trace how the properties of the PAHs vary in comparison with multi-wavelength tracers of the phase of the ISM.

2. Data

2.1. JWST–MIRI Maps Tracing the 7.7 and 11.3 μm Bands

We use the MIRI F770W and F1130W maps of three early targets in the PHANGS–JWST Treasury program #2107 (PI: Lee): NGC 628, NGC 1365, and NGC 7496. Description of the data reduction for the MIRI images can be found in Lee et al. (2023). Since we are interested in the diffuse PAH emission throughout the maps, the background level and the uncertainty in the maps are critical. The background level was tied to larger archival Spitzer and Wide-field Infrared Survey Explorer (WISE) maps of the targets with well-covered "off" galaxy regions (see Appendices A and B in Leroy et al. 2023). As shown in Figure 1, the F770W and F1130W were ideally designed to sample the 7.7 and 11.3 μm PAH emission complexes. The filter transmission curves are shown as colored lines with labels on the right, and the shaded areas help visualize the fraction of each complex that is included in the

filters used here. For visual comparison purposes, we indicate with vertical lines the "clip points" used in Draine et al. (2021). In this Letter, the F770W and F1130W values we use are the instrument's filter-integrated fluxes.

All maps were convolved to the point-spread function (PSF) of the F1130W filter (FWHM $\sim 0\farcs36$) using a standard convolution procedure, with kernels generated following the approach of Aniano et al. (2011). All maps were also aligned to the same astrometric grid, with pixels size $\sim 0\farcs11$.

Although the F770W and F1130W bands are dominated by the 7.7 and 11.3 μm PAH emission features, both can also include some hot dust and/or continuum emission, especially toward bright H II regions. C. M. Whitcomb et al. (2023, in preparation) used PAHFIT (Smith et al. 2007) to show that the Spitzer/IRS spectra of the star-forming regions in the SINGS sample, which are among the brightest in these galaxies, may have $\sim$30% continuum contamination in F1130W and $\sim$10% in F770W, although these measurements rely on models of mid-IR emission that will likely be updated with new JWST results. Note that H II regions are the place where contamination from hot dust is the highest. Naturally, a more detailed analysis and correction will be the subject of further study.

In addition to continuum contamination, it is also possible that silicate absorption at 9.7 μm could reduce the F1130W flux. Smith et al. (2007) show that this absorption should not play a large role in most star-forming galaxies. Additionally, Groves et al. (2023) also find that a median $E(B-V) \sim$ 0.2–0.3 for H II regions in the four targets in this work, is a relatively low value. At this point, we therefore do not considered silicate absorption in this early work.

2.2. JWST–NIRCam Maps Tracing the 3.3 μm Band

We use the 3.3 μm emission maps from Sandstrom et al. (2023). They use a combination of the NIRCam F335M (measuring the main PAH emission feature), and the F300M plus F360M filters to remove starlight continuum. They base their continuum removal approach on the prescription from Lai et al. (2020), with additional corrections to avoid over-subtraction of the PAH emission in regions where the map is ISM emission dominated rather than stellar continuum dominated in the F360M filter.[26] Lai et al. (2020) show contamination from emission lines is negligible in the F335M band. For full details on the removal of contamination from starlight in the F335M band, we refer to Sandstrom et al. (2023), which includes robust discussion of any potential remaining contamination that could artificially raise the $\mathrm{F335M_{PAH}}$. We refer to these final maps that isolate the emission from the 3.3 μm emission complex as $\mathrm{F335M_{PAH}}$. We convolve these maps to the F1130W PSF using the same approach as the other maps, as described above.

2.3. Ancillary Data

We combine CO, HI, and Hα measurements to trace the conditions of the ISM in our targets. We use the same CO/HI/Hα data as the companion letter on PAH fraction (Chastenet et al. 2023). We trace the molecular gas content using CO data from the PHANGS–ALMA survey (Leroy et al. 2021a, 2021b). We convert ^{12}CO $(2-1)$ measurements to H_2 surface density using the Milky Way CO-to-H_2 conversion factor $\alpha_{CO} = 4.35\ M_\odot$ pc^{-2} (K km s^{-1})$^{-1}$, and a ^{12}CO$(2-1)$ to ^{12}CO$(1-0)$ line ratio $R_{21} = 0.65$ (den Brok et al. 2021; Leroy et al. 2022). We use HI data from the PHANGS–MeerKAT survey (C. Eibensteiner et al., in preparation) and THINGS (Walter et al. 2008) surveys, assuming optically thin 21 cm emission, and using a conversion factor of $0.020\ M_\odot$ pc^{-2} (K km s^{-1})$^{-1}$ (Leroy et al. 2012, see also Walter et al. 2008). We do not convolve the JWST and other data sets to match the 11″–15″ HI resolution. We assume that the HI is smoothly distributed below the MeerKAT and THINGS resolution, as suggested by observations of more nearby targets (Leroy et al. 2013). There are currently no available 21 cm observations for NGC 1365, so we assume it to have a uniform neutral gas surface density of $8\ M_\odot$ pc^{-2} everywhere, based on the observed flatness of the atomic gas distribution in the disks of galaxies (e.g., Schruba et al. 2011; Bigiel & Blitz 2012; Kennicutt & Evans 2012; Wong et al. 2013). We trace ionized gas using the Hα data (not extinction corrected) from the PHANGS–MUSE observations (Emsellem et al. 2022).

2.4. Noise Properties and Masks

After convolution to the F1130W PSF, we measure a background standard deviation of $\sim$0.065 MJy sr^{-1} in the MIRI F770W map of NGC 7496. It is the only target that provides sufficiently empty space to measure a background without significant contamination from the source. We use that value to perform signal-to-noise (S/N) cuts in all three galaxies, and we exclude pixels with S/N $\leqslant 3$ in the MIRI maps. All MIRI maps have similar noise from the pipeline, verified with moderate masking, so it therefore is reasonable to assume the convolved maps show similar noise. We consequently base our noise estimate off the convolved map of NGC 7496.

After convolution, we measure a noise in the $\mathrm{F335M_{PAH}}$ maps of $\sim$0.014 MJy sr^{-1} in NGC 7496. Similarly, we use that value in all three targets to perform cuts and remove pixels with S/N $\leqslant 3$ in the $\mathrm{F335M_{PAH}}$ maps. Figures 2 through 4 show the remaining pixels in the three targets.

Since NGC 1365 and NGC 7496 have saturated central sources that cause contamination of the surrounding maps by the PSF wings, we use the instrument PSF of the F1130W filter to mask the saturated and contaminated pixels in these galaxy centers.

3. Band Ratios

We present maps of the $\mathrm{F335M_{PAH}}$/F770W, $\mathrm{F335M_{PAH}}$/F1130W, and F1130W/F770W band ratios in NGC 628 (Figure 2), NGC 1365 (Figure 3), and NGC 7496 (Figure 4). The color scale for each band ratio is the same across the three figures, with limits chosen using the fifth and 95th percentiles of all values. We overlay the H II regions cataloged in Groves et al. (2023) and Santoro et al. (2022) with black contours.

Overall, each ratio shows variations both within and across galaxies, spanning values within a factor of 4–5 for $\mathrm{F335M_{PAH}}$/F770W and $\mathrm{F335M_{PAH}}$/F1130W, and less than a factor of 2 in the F1130W/F770W maps. Table 1 lists the mean, median, and 16th–84th percentile ranges of the three ratios in each galaxy. These values are also well illustrated in Figure 5. The mean and median values in $\mathrm{F335M_{PAH}}$/F770W and $\mathrm{F335M_{PAH}}$/F1130W increase from NGC 628, to NGC 1365, and to NGC 7496, which shows the highest ratios. The 16th–84th percentile ranges between NGC 628 and NGC 7496 barely overlap, indicating a real offset between these two galaxies in the

[26] Note that an additional factor would be required to convert $\mathrm{F335M_{PAH}}$ from MJy sr^{-1} into an integrated band intensity (see Lai et al. 2020).

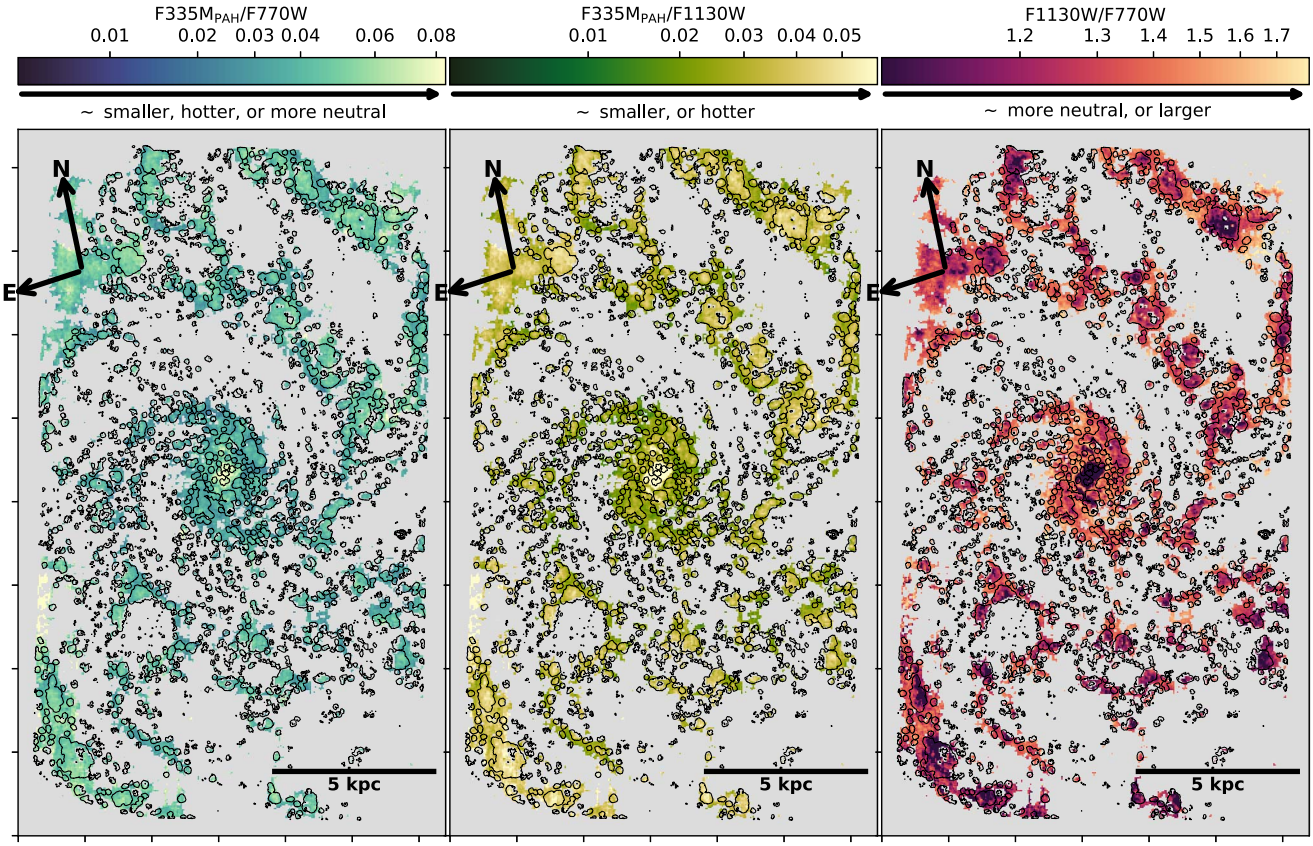

Figure 2. PAH band ratios in NGC 628. The maps show all pixels passing S/N $\geqslant 3$ in all bands (see Section 2.4). The F335M$_{\rm PAH}$ refers to the 3.3 μm maps developed by Sandstrom et al. (2023). The contour show the H II regions from the nebula catalog by Groves et al. (2023) and Santoro et al. (2022). (The maps were arbitrarily rotated from north-up to allow for better visualization.)

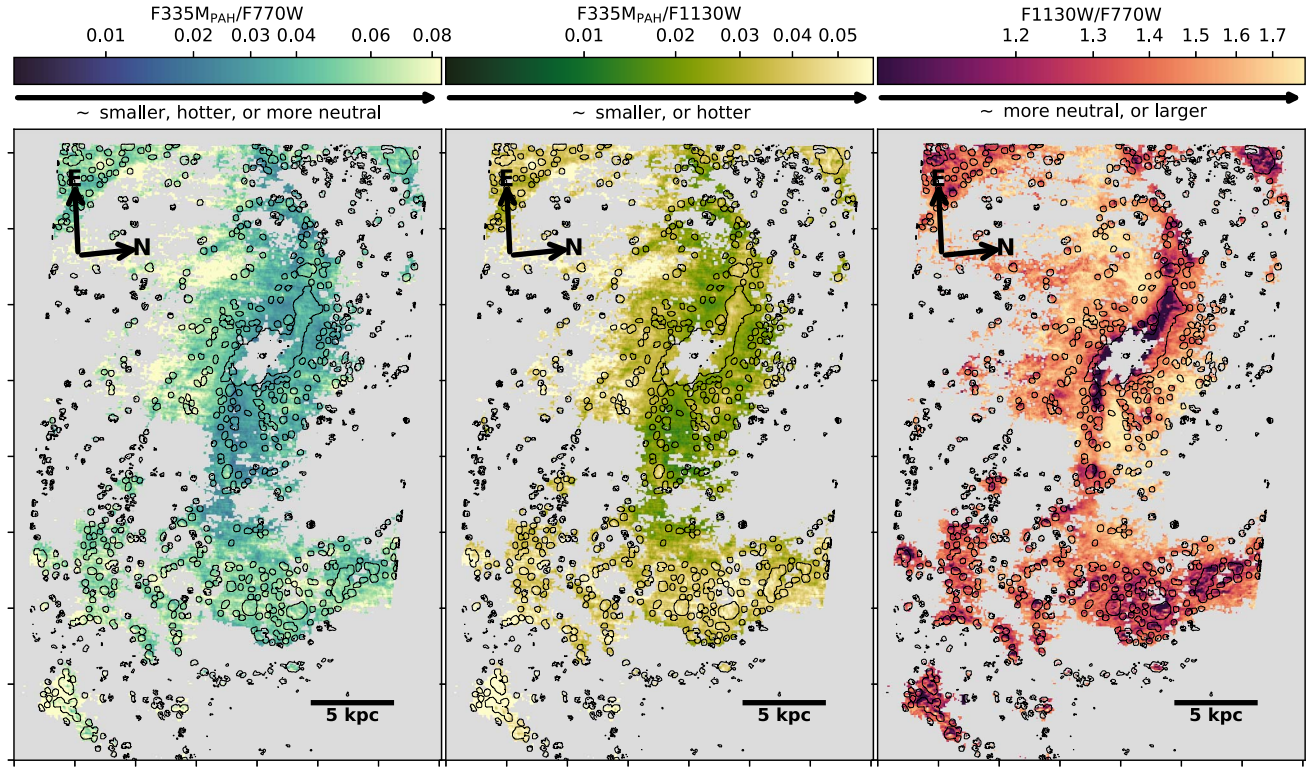

Figure 3. Same as Figure 2 for NGC 1365. The central pixels are masked due to saturation, using the PSF at F1130W. The visible stripes are due to $1/f$ noise in the NIRCam bands. (The maps were arbitrarily rotated from north-up to allow for better visualization.)

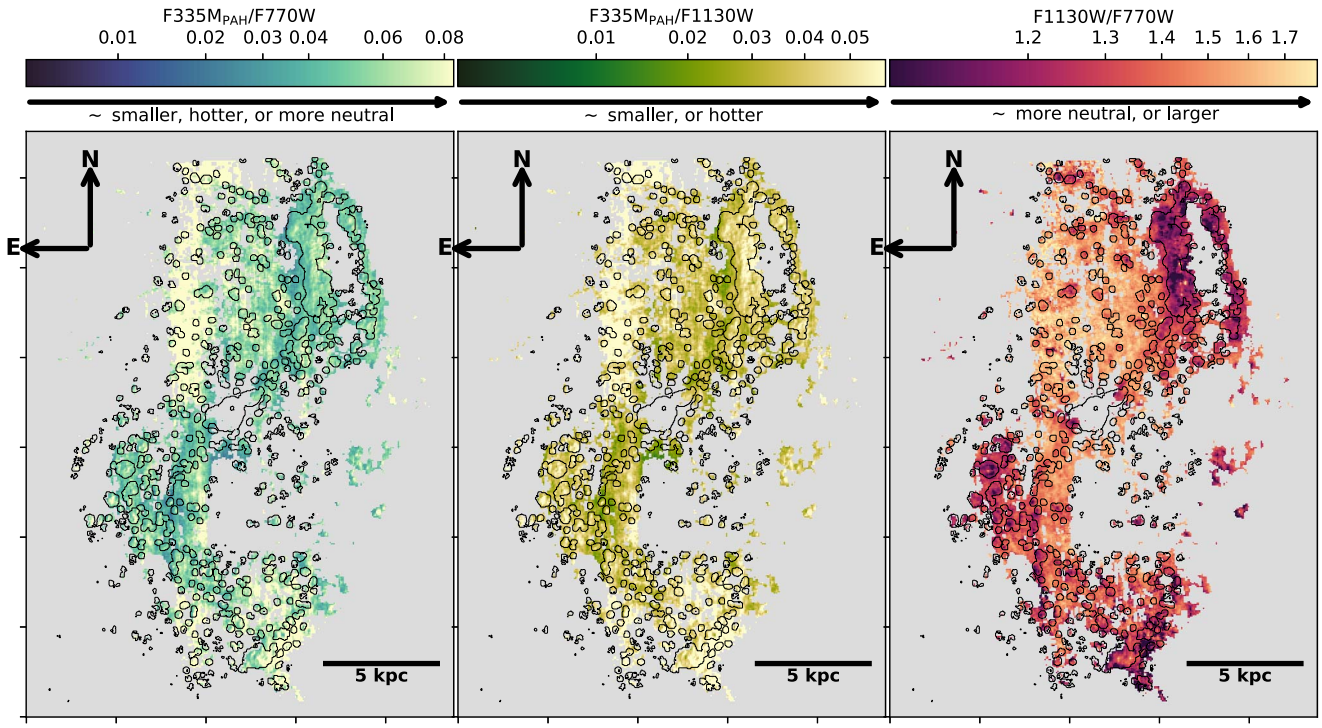

Figure 4. Same as Figure 2 for NGC 7496. The central pixels are masked due to saturation, using the PSF at F1130W. The visible stripes are due to $1/f$ noise in the NIRCam bands.

Table 1
Means, Medians, and 16th and 84th Percentiles for the Three Ratios F335M$_{PAH}$/F770W (left), F335M$_{PAH}$/F1130W (Center), and F1130W/F770W (Right), in Each Galaxy

Galaxy	F335M$_{PAH}$/F770W			F335M$_{PAH}$/F1130W			F1130W/F770W		
	Mean	Median	16th–84th Perc.	Mean	Median	16th–84th Perc.	Mean	Median	16th–84th Perc.
NGC 628	0.043	0.039	0.028 – 0.054	0.032	0.029	0.02 – 0.042	1.38	1.37	1.20 – 1.56
NGC 1365	0.061	0.053	0.035 – 0.084	0.042	0.037	0.023 – 0.058	1.48	1.48	1.27 – 1.69
NGC 7496	0.067	0.057	0.040 – 0.092	0.049	0.041	0.029 – 0.065	1.41	1.40	1.22 – 1.60

Note. While the 16th–84th percentile ranges of F1130W/F770W overlap between targets, the other ratios with F335M$_{PAH}$ seem to show more distinct values.

F335M$_{PAH}$/F770W and F335M$_{PAH}$/F1130W ratios. On the other hand, all three galaxies show relatively similar mean and median values of the F1130W/F770W ratio, with significant overlap in 16th–84th ranges. This suggests that, in terms of band ratios, the main difference between each galaxy is driven by the emission from the 3.3 μm complex, traced by F335M$_{PAH}$ (see also Sandstrom et al. 2023).

The ratio maps show higher values of the F335M$_{PAH}$/F770W and F335M$_{PAH}$/F1130W ratios in H II regions. This is clearly visible in NGC 628 and NGC 7496, and slightly less obvious in NGC 1365 though still distinguishable. This indicates enhanced 3.3 μm emission in these regions compared to the other two PAH features. In all galaxies, the F1130W/F770W maps show darker colors in H II regions, pointing to increased average PAH ionization likely driven by the proximity of young stellar populations. This is similar to what is seen in Dale et al. (2023), which examines the properties of the PAHs within compact stellar clusters and finds a positive correlation between cluster age and PAH ionization. In the galaxy NGC 1365, darker colors in the right panel of Figure 3 (i.e., lower values of F1130W/F770W), tracing more ionized PAHs, can be found in the dust lanes. This is also visible in NGC 7496.

The relative prominence of the 3.3 μm feature in H II regions could suggest that PAHs in these regions are smaller, and/or hotter than in the surrounding diffuse ISM. The emission in the 3.3 μm is usually attributed to small PAHs. In this case, the higher F335M$_{PAH}$/F770W and F335M$_{PAH}$/F1130W would suggest smaller PAHs in H II regions. But the seemingly higher fraction of smaller PAHs in harsh environments is not supported by theoretical studies, which have shown that smaller PAHs have shorter lifetimes in a hot gas (e.g., Micelotta et al. 2010). However, it is important to note that in the vicinity of H II regions with harder radiation fields, PAHs will be hotter due to an increase in the average energy of the photons. An increase in dust temperature naturally shifts the power in the emission spectrum toward shorter wavelengths; in this case, hotter PAHs would lead to more power in the 3.3 μm feature, interpreted as an apparent shift toward smaller sizes (Draine et al. 2021). This shift is clearly demonstrated in Figure 21, panel (d) of Draine et al. (2021), in which the value of $F_{clip}(3.3)/F_{clip}(11.2)$ irradiated by a Galactic radiation field (mMMP) is approximately a factor of 2 lower than the $F_{clip}(3.3)/F_{clip}(11.2)$ irradiated by a young stellar population (BC03, 3Myr). We note that the shift reported by the models is

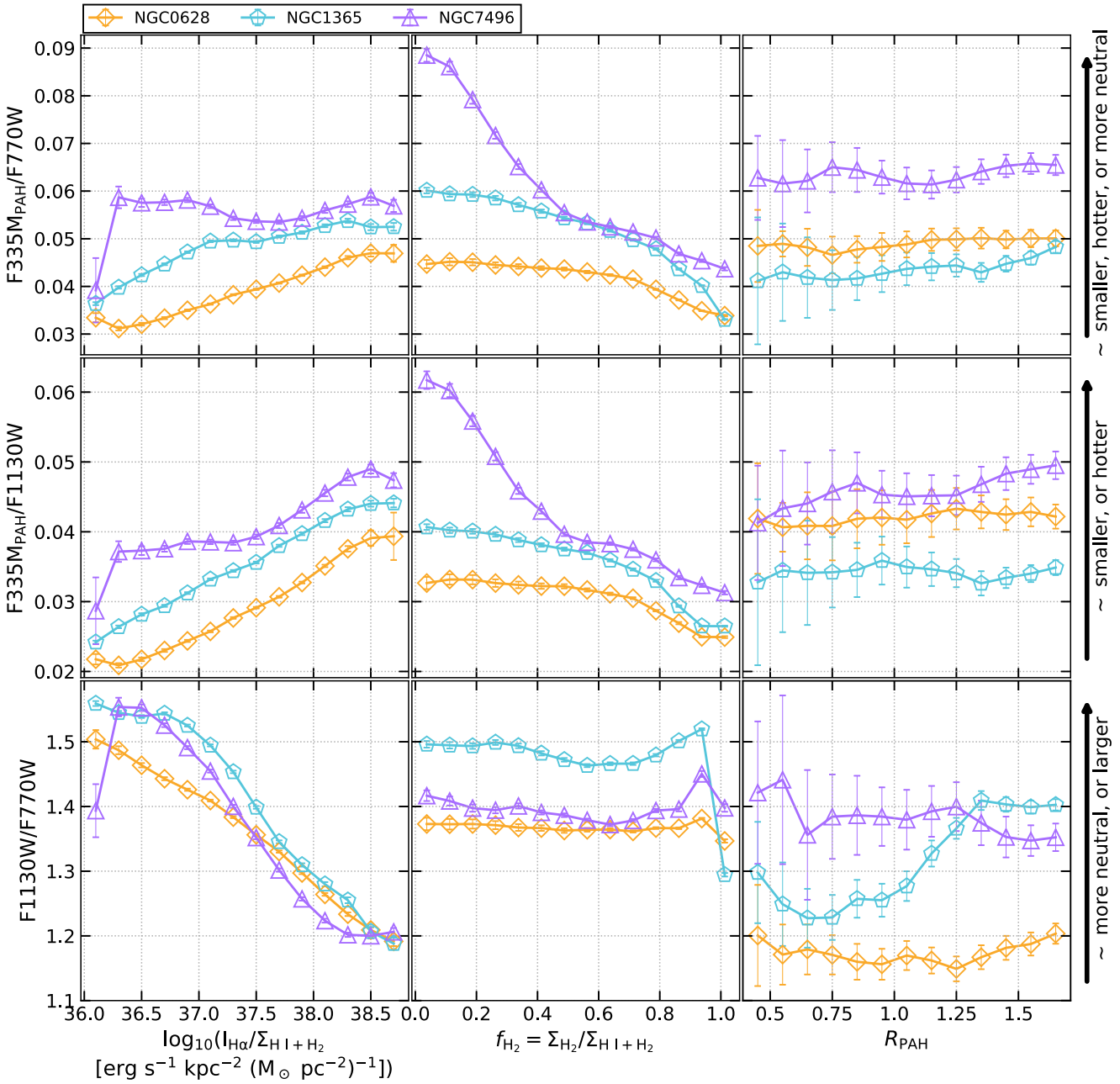

Figure 5. Running medians of the F335M$_{PAH}$/F770W (top), F335M$_{PAH}$/F770W (middle), and F1130W/F770W (bottom), in bins of $I_{H\alpha}/\Sigma_{HI+H_2}$ (left), fraction of molecular gas, f_{H_2} (right), and the abundance ratio R_{PAH} = (F700W+F1130W)/F2100W.

smaller than the shift we see in the H II regions across the galaxies presented here, suggesting potential additional factors not accounted for in the Draine et al. (2021) models.

The combined analysis of these three galaxies also indicates that the F1130W/F770W ratios are lowest in H II regions, the star-forming arms, and gas and dust lanes that may include shocked gas. This argues that the fraction of ionized PAHs surrounding sites of active star formation are on average higher than in the diffuse ISM. This is further discussed in Egorov et al. (2023), which examines the PAH emission in H II regions. The relative consistency of the ratios in the interarm ISM where detected, despite sampling three different galaxies, implies that PAHs permeate the diffuse ISM and have similar properties throughout this ISM phase.

Note that we attribute the high F335M$_{PAH}$/F770W and F335M$_{PAH}$/F1130W in the inner 200 pc ($\sim$4″) of NGC 628 to the very low ISM contribution in that region, and not a change in PAH properties (e.g., Dale et al. 2006; Hoyer et al. 2023).

4. Variation of Band Ratios with ISM Environment

In Figure 5, we show the variations of the three ratios, F335M$_{PAH}$/F770W (top row), F335M$_{PAH}$/F1130W (middle row), and F1130W/F770W (bottom row), as a function of $I_{H\alpha}/\Sigma_{HI+H_2}$ in units of erg s^{-1} kpc^{-2} ($M_\odot$ pc^{-2})$^{-1}$ (left column), and fraction of molecular gas (right column). The symbols are the medians in each bin of the x-axis, and the error bars show 3 standard errors of the mean.

All ratios show clear variations with the ionized gas content, as shown in the first column. The first two ratios are sensitive to

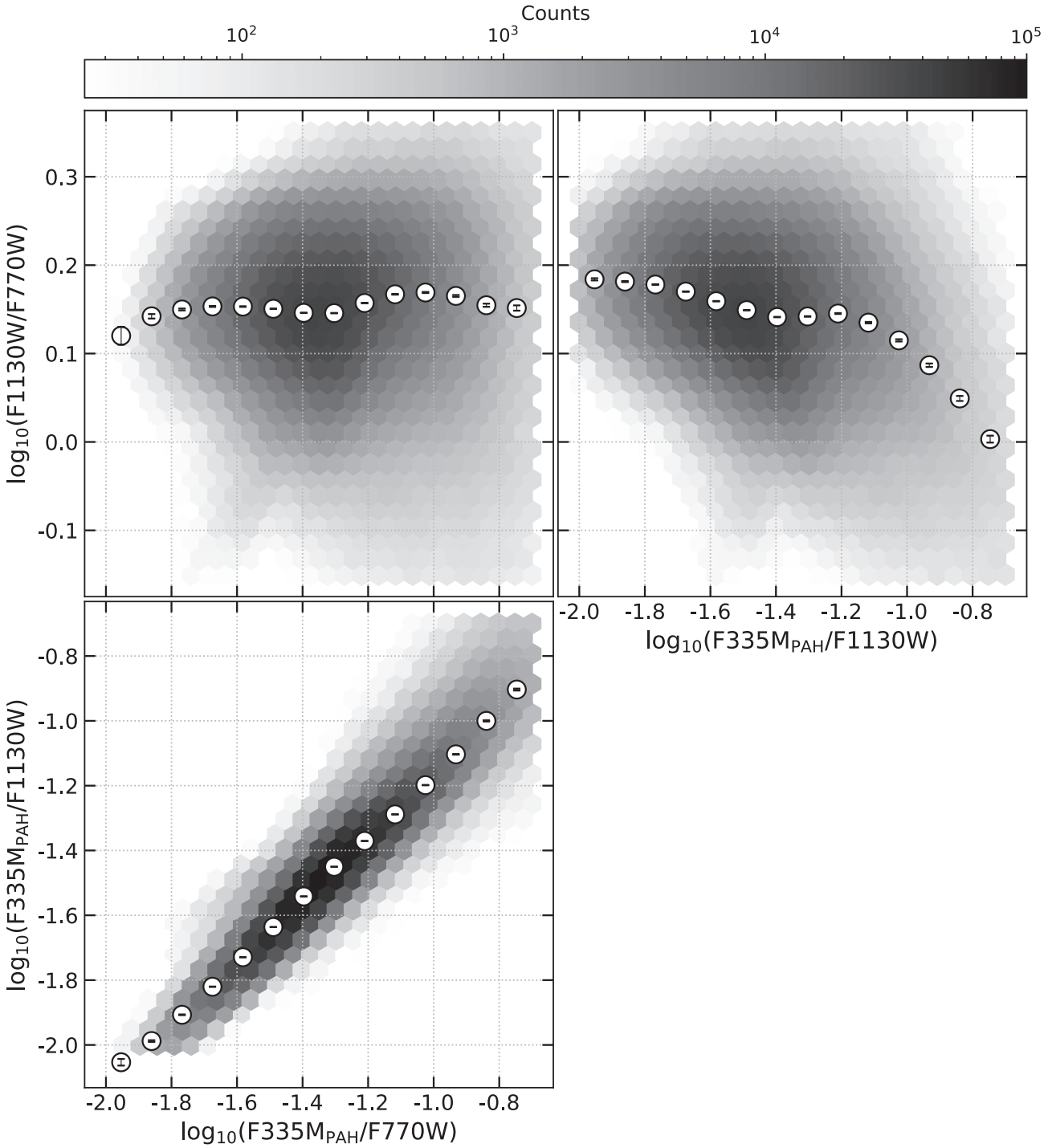

Figure 6. 2D histograms of the F335M$_{\rm PAH}$/F770W vs. F1130W/F770W (top), and F335M$_{\rm PAH}$/F770W vs. F335M$_{\rm PAH}$/F1130W (bottom). Both ratios in the bottom panel trace the size of PAHs, and show a clear correlation. In the top panel, the *x*-axis traces size, while the *y*-axis traces ionization.

the global size of the PAHs, and increase with $I_{\rm H\alpha}/\Sigma_{\rm HI+H_2}$. This suggests that the PAH population decreases to lower sizes as the ionized gas becomes more prominent, though heating could also drive this observed change (as discussed in Section 3). The F1130W/F770W ratio, on the other hand, decreases at high values of $I_{\rm H\alpha}/\Sigma_{\rm HI+H_2}$, which suggests that the PAHs are more ionized with a higher fraction of ionized gas to total gas. Both these trends are consistent with the expected first-order effect from hot gas, which should be able to fragment PAHs or kick electrons. However, there is also a known negative effect of ionized gas on the global PAH abundance (e.g., Micelotta et al. 2010; Chastenet et al. 2019). The last column of Figure 5 shows the variations of the "abundance ratio," $R_{\rm PAH} = ({\rm F770W} + {\rm F1130W})/{\rm F2100W}$ tracing the global PAH abundance[27] (see also letters from Chastenet et al. 2023; Egorov et al. 2023). In these panels,

[27] To first-order, (7.7+11.3)/21 traces PAH abundance, as was seen by the equivalent 8/24 μm that was frequently used in Spitzer observations (e.g., Engelbracht et al. 2006; Draine & Li 2007; Engelbracht et al. 2008). In our early results, we are focused on observed ratios, rather than modeling. Any exact relationship between the PAH fraction and the ratio used to measure $R_{\rm PAH}$ will be left to future studies.

neither of the ratios show a strong trend with $R_{\rm PAH}$. Chastenet et al. (2023) show that $R_{\rm PAH}$ clearly decreases with $I_{\rm H\alpha}/\Sigma_{\rm HI+H_2}$, but no clear variation is seen with size or ionization tracers.

The second column shows the variations of the three ratios with the fraction of molecular gas, $f_{\rm H_2} \equiv \Sigma_{\rm H_2}/(\Sigma_{\rm HI} + \Sigma_{\rm H_2})$. Both ratios tracing the size of PAHs (F335M$_{\rm PAH}$/F770W, and F335M$_{\rm PAH}$/F1130W) show a steep decrease with $f_{\rm H_2}$ in NGC 7496, and a much shallower trend in NGC 0628 and NGC 1365. In the bottom-center panel, however, while all curves show similar trends, only NGC 1365 differs from NGC 628, while NGC 7496 show identical values over a large range of $f_{\rm H_2}$. While NGC 1365 clearly has a higher CO content, NGC 628 and NGC 7496 show similar $L_{\rm CO}$ values (Leroy et al. 2021b). Additionally, note that both NGC 1365 and NGC 7496 host an AGN in their center. The variations shown in the center column could indicate that: (1) the presence of an AGN has a stronger effect on the size of PAHs rather than their ionization, and (2) the CO content will have the opposite effect, with a higher impact on ionization rather than size. However, these two Seyfert galaxies show different trends, making it difficult to clearly determine the effect of an AGN on the PAH population at this stage.

In Figure 6 we show the 2D histograms of all three ratios with each other, with the associated running medians and error bars showing three standard errors of the mean. In the bottom panel, the F335M$_{\rm PAH}$/F770W and F335M$_{\rm PAH}$/F1130W appear clearly correlated, which is expected as they are both tracers of the global size distribution of PAHs.[28] In the top row, the F1130W/F770W as a function of F335M$_{\rm PAH}$/F770W (left) shows a rather flat distribution. In the right panel, F1130W/F770W seems to gently decrease with F335M$_{\rm PAH}$/F1130W (though the large scatter can be consistent with a flat trend). The lack of a clear trend between F1130W/F770W and the other ratios is interesting as it suggests that ionization and size do not strongly vary together. A clear interpretation of the difference between the two panels in the top row requires a clear understanding of the different populations traced by F335M$_{\rm PAH}$/F770W and F335M$_{\rm PAH}$/F1130W.

5. Conclusions

Data from JWST provide exciting opportunities for understanding the ISM conditions of galaxies outside the Milky Way at ∼10 pc resolution. In particular, the MIRI and NIRCam instruments are able to capture the strength of important PAH features that can be used to assess the properties of these dust grains. Studies of the PAH population in nearby galaxies have shown the PAHs have an important impact on other evolution processes, as they can be used as a star formation rate tracer and are heavily responsible for the photoelectric heating of the gas. Through analysis of the ratio of the 11.3 to the 7.7 μm PAH features, changes in the ionization fraction of the PAHs can be determined, while the strength of the 3.3 μm compared to the 7.7 μm or 11.3 μm features provides information on the average PAH size.

We present maps of these ratios across nearby galaxies NGC 628, NGC 1365, and NGC 7496. Based on the relative consistency of these ratios across each galaxy disk, we conclude that the population of PAHs is fairly uniform. H II regions and star-forming spiral arms show lower 11.3/7.7 and higher F335M$_{\rm PAH}$/F1130W values, indicating the presence of smaller, highly charged grains in these regions. The trends in these ratios are further discussed in Dale et al. (2023), where each ratio is measured in a sample of over 1000 stellar clusters. In addition, the trends observed between the state of the gas measured by $f_{\rm H_2}$ and $I_{\rm H\alpha}/\Sigma_{\rm HI+H_2}$ show that local gas conditions can greatly impact the sizes and ionization levels of the PAHs: more ionized (traced by F1130W/F770W) and smaller PAHs (traced by F335M$_{\rm PAH}$/F770W and F335M$_{\rm PAH}$/F1130W) are present in regions showing high Hα intensity.

This work highlights the diagnostic power of JWST–MIRI and NIRCam observations of nearby galaxies. By probing previously inaccessible spatial scales and emission levels, we can better assess the physical mechanisms that link PAH grains and their local environment. Further work to determine how these PAH feature ratios are influenced by stellar population age, gas–phase metallicity, and other galactic-scale and ISM properties will shed light on the delicate interplay between stars, gas, and dust in galaxies.

We thank the anonymous referee for their careful reading and comments that helped improve the clarity of the Letter. This work was carried out as part of the PHANGS collaboration, associated with JWST program 2107. This work is based on observations made with the NASA/ESA/CSA JWST. Some/all of the data presented in this Letter were obtained from the Mikulski Archive for Space Telescopes (MAST) at the Space Telescope Science Institute, which is operated by the Association of Universities for Research in Astronomy, Inc., under NASA contract NAS 5-03127. The specific observations analyzed can be accessed via doi:10.17909/9bdf-jn24. Based on observations collected at the European Southern Observatory under ESO programmes 094.C-0623 (PI: Kreckel), 095.C-0473, 098.C-0484 (PI: Blanc), 1100.B-0651 (PHANGS–MUSE; PI: Schinnerer), as well as 094.B-0321 (MAGNUM; PI: Marconi), 099.B-0242, 0100.B-0116, 098.B-0551 (MAD; PI: Carollo), and 097.B-0640 (TIMER; PI: Gadotti). This Letter makes use of the following ALMA data:

ADS/JAO.ALMA#2012.1.00650.S,
ADS/JAO.ALMA#2013.1.01161.S,
ADS/JAO.ALMA#2015.1.00925.S,
ADS/JAO.ALMA#2015.1.00956.S,
ADS/JAO.ALMA#2017.1.00392.S,
ADS/JAO.ALMA#2017.1.00766.S,
ADS/JAO.ALMA#2017.1.00886.L,
ADS/JAO.ALMA#2018.1.01651.S,
ADS/JAO.ALMA#2018.A.00062.S.

ALMA is a partnership of ESO (representing its member states), NSF (USA) and NINS (Japan), together with NRC (Canada), MOST and ASIAA (Taiwan), and KASI (Republic of Korea), in cooperation with the Republic of Chile. The Joint ALMA Observatory is operated by ESO, AUI/NRAO, and NAOJ.

J.C. acknowledges support from ERC starting grant No. 851622 DustOrigin. E.J.W. acknowledges funding from the Deutsche Forschungsgemeinschaft (DFG, German Research Foundation)—Project-ID 138713538—SFB 881 ("The Milky Way System," subproject P1). H.A.P. acknowledges support by the National Science and Technology Council of Taiwan under grant 110-2112-M-032-020-MY3. M.C. gratefully acknowledges funding from the DFG through an Emmy

[28] We note that the bulk of the F335M$_{\rm PAH}$/F1130W distribution is lower than the one found in Sandstrom et al. (2023). This is likely due to the convolution to F1130W resolution, which leads to including more pixels in the diffuse regions, with lower F335M$_{\rm PAH}$ values.

Noether Research Group (grant No. CH2137/1-1). COOL Research DAO is a Decentralized Autonomous Organization supporting research in astrophysics aimed at uncovering our cosmic origins. J.M.D.K. gratefully acknowledges funding from the European Research Council (ERC) under the European Union's Horizon 2020 research and innovation program via the ERC Starting Grant MUSTANG (grant agreement No. 714907). T.G.W. acknowledges funding from the European Research Council (ERC) under the European Union's Horizon 2020 research and innovation program (grant agreement No. 694343). M.B. acknowledges support from FONDECYT regular grant 1211000 and by the ANID BASAL project FB210003. K.K., O.E. gratefully acknowledge funding from the Deutsche Forschungsgemeinschaft (DFG, German Research Foundation) in the form of an Emmy Noether Research Group (grant No. KR4598/2-1, PI Kreckel). F.B. would like to acknowledge funding from the European Research Council (ERC) under the European Union's Horizon 2020 research and innovation program (grant agreement No.726384/Empire). M.Q. acknowledges support from the Spanish grant PID2019-106027GA-C44, funded by MCIN/AEI/10.13039/501100011033. E.R. and H.H. acknowledge the support of the Natural Sciences and Engineering Research Council of Canada (NSERC), funding reference number RGPIN-2022-03499. K.G. is supported by the Australian Research Council through the Discovery Early Career Researcher Award (DECRA) Fellowship DE220100766 funded by the Australian Government. K.G. is supported by the Australian Research Council Centre of Excellence for All Sky Astrophysics in 3 Dimensions (ASTRO 3D), through project number CE170100013. A.K.L. gratefully acknowledges support by grants 1653300 and 2205628 from the National Science Foundation, by award JWST-GO-02107.009-A, and by a Humboldt Research Award from the Alexander von Humboldt Foundation.

Facilities: JWST (NIRCam, MIRI), MUSE, ALMA.

ORCID iDs

Jérémy Chastenet https://orcid.org/0000-0002-5235-5589
Jessica Sutter https://orcid.org/0000-0002-9183-8102
Karin Sandstrom https://orcid.org/0000-0002-4378-8534
Francesco Belfiore https://orcid.org/0000-0002-2545-5752
Oleg V. Egorov https://orcid.org/0000-0002-4755-118X
Kirsten L. Larson https://orcid.org/0000-0003-3917-6460
Adam K. Leroy https://orcid.org/0000-0002-2545-1700
Daizhong Liu https://orcid.org/0000-0001-9773-7479
Erik Rosolowsky https://orcid.org/0000-0002-5204-2259
David A. Thilker https://orcid.org/0000-0002-8528-7340
Elizabeth J. Watkins https://orcid.org/0000-0002-7365-5791
Thomas G. Williams https://orcid.org/0000-0002-0786-7307
Ashley. T. Barnes https://orcid.org/0000-0003-0410-4504
F. Bigiel https://orcid.org/0000-0003-0166-9745
Médéric Boquien https://orcid.org/0000-0003-0946-6176
Mélanie Chevance https://orcid.org/0000-0002-5635-5180
Daniel A. Dale https://orcid.org/0000-0002-5782-9093
J. M. Diederik Kruijssen https://orcid.org/0000-0002-8804-0212
Eric Emsellem https://orcid.org/0000-0002-6155-7166
Kathryn Grasha https://orcid.org/0000-0002-3247-5321
Brent Groves https://orcid.org/0000-0002-9768-0246
Hamid Hassani https://orcid.org/0000-0002-8806-6308
Annie Hughes https://orcid.org/0000-0002-9181-1161
Kathryn Kreckel https://orcid.org/0000-0001-6551-3091
Sharon E. Meidt https://orcid.org/0000-0002-6118-4048
Hsi-An Pan https://orcid.org/0000-0002-1370-6964
Miguel Querejeta https://orcid.org/0000-0002-0472-1011
Eva Schinnerer https://orcid.org/0000-0002-3933-7677
Cory M. Whitcomb https://orcid.org/0000-0003-2093-4452

References

Allamandola, L. J., Tielens, A. G. G. M., & Barker, J. R. 1985, ApJL, 290, L25
Allamandola, L. J., Tielens, G. G. M., & Barker, J. R. 1989, ApJS, 71, 733
Aniano, G., Draine, B. T., Gordon, K. D., & Sandstrom, K. 2011, PASP, 123, 1218
Bakes, E. L. O., & Tielens, A. G. G. M. 1994, ApJ, 427, 822
Bauschlicher, C. W., Ricca, A., Boersma, C., & Allamandola, L. J. 2018, ApJS, 234, 32
Bigiel, F., & Blitz, L. 2012, ApJ, 756, 183
Boersma, C., Bregman, J., & Allamandola, L. J. 2016, ApJ, 832, 51
Boersma, C., Bregman, J., & Allamandola, L. J. 2018, ApJ, 858, 67
Boersma, C., Bauschlicher, C. W. J., Ricca, A., et al. 2014, ApJS, 211, 8
Chastenet, J., Sandstrom, K., Chiang, I.-D., et al. 2019, ApJ, 876, 62
Chastenet, J., Sutter, J., Sandstrom, K. M., et al. 2023, ApJL, 944, L11
Croxall, K. V., Smith, J. D., Wolfire, M. G., et al. 2012, ApJ, 747, 81
Dale, D. A., Boquien, M., Barnes, A., et al. 2023, ApJL, 944, L23
Dale, D. A., Smith, J. D. T., Armus, L., et al. 2006, ApJ, 646, 161
den Brok, J. S., Chatzigiannakis, D., Bigiel, F., et al. 2021, MNRAS, 504 3221
Draine, B. T., & Li, A. 2001, ApJ, 551, 807
Draine, B. T., & Li, A. 2007, ApJ, 657, 810
Draine, B. T., Li, A., Hensley, B. S., et al. 2021, ApJ, 917, 3
Egorov, O., Kreckel, K., Sandstrom, K. M., et al. 2023, ApJL, 944, L16
Emsellem, E., Schinnerer, E., Santoro, F., et al. 2022, A&A, 659, A191
Engelbracht, C. W., Rieke, G. H., Gordon, K. D., et al. 2008, ApJ, 678, 804
Engelbracht, C. W., Kundurthy, P., Gordon, K. D., et al. 2006, ApJL, 642, L127
Galliano, F., Madden, S. C., Tielens, A. G. G. M., Peeters, E., & Jones, A. P. 2008, ApJ, 679, 310
Hoyer, N., Pinna, F., Kamlah, A. W. H., et al. 2023, ApJL, 944, L25
Gillett, F. C., Forrest, W. J., & Merrill, K. M. 1973, ApJ, 183, 87
Groves, B., Kreckel, K., Santoro, F., et al. 2023, arXiv:2301.03811
Jones, A. P., Kohler, M., Ysard, N., Bocchio, M., & Verstraete, L. 2017, A&A, 602, A46
Kennicutt, R. C., & Evans, N. J. 2012, ARA&A, 50, 531
Kerkeni, B., Garcia-Bernete, I., Rigopoulou, D., et al. 2022, MNRAS, 513, 3663
Lai, T. S.-Y., Smith, J. D. T., Baba, S., Spoon, H. W. W., & Imanishi, M. 2020, ApJ, 905, 55
Le Bourlot, J., Le Petit, F., Pinto, C., Roueff, E., & Roy, F. 2012, A&A, 541, A76
Le Page, V., Snow, T. P., & Bierbaum, V. M. 2009, ApJ, 704, 274
Lee, J. C., Sandstrom, K. M., Leroy, A. K., et al. 2023, ApJL, 944, L17
Leger, A., & Puget, J. L. 1984, A&A, 137, L5
Leroy, A. K., Bigiel, F., de Blok, W. J. G., et al. 2012, AJ, 144, 3
Leroy, A. K., Lee, C., Schruba, A., et al. 2013, ApJL, 769, L12
Leroy, A. K., Hughes, A., Liu, D., et al. 2021a, ApJS, 255, 19
Leroy, A. K., Sandstrom, K. M., Rosolowsky, E. W., et al. 2023, ApJL, 944, L9
Leroy, A. K., Schinnerer, E., Hughes, A., et al. 2021b, ApJS, 257, 43
Leroy, A. K., Rosolowsky, E., Usero, A., et al. 2022, ApJ, 927, 149
Li, A. 2020, NatAs, 4, 339
Maragkoudakis, A., Boersma, C., Temi, P., Bregman, J. D., & Allamandola, L. J. 2022, ApJ, 931, 38
Maragkoudakis, A., Peeters, E., & Ricca, A. 2020, MNRAS, 494, 642
Mattioda, A. L., Hudgins, D. M., Boersma, C., et al. 2020, ApJS, 251, 22
McKinney, J., Armus, L., Pope, A., et al. 2021, ApJ, 908, 238
Merrill, R. M., Soifer, B. T., & Russell, R. W. 1975, ApJL, 200, L37
Micelotta, E. R., Jones, A. P., & Tielens, A. G. G. M. 2010, A&A, 510, A37
Rieke, G. H., Wright, G. S., Boker, T., et al. 2015, PASP, 127, 584
Rieke, M. J., Kelly, D., & Horner, S. 2005, Proc. SPIE, 5904, 1
Rigopoulou, D., Barale, M., Clary, D. C., et al. 2021, MNRAS, 504, 5287
Sandstrom, K. M., Bolatto, A. D., Bot, C., et al. 2012, ApJ, 744, 20

Sandstrom, K. M., Chastenet, J., Sutter, J., et al. 2023, ApJL, 944, L7
Santoro, F., Kreckel, K., Belfiore, F., et al. 2022, A&A, 658, A188
Schruba, A., Leroy, A. K., Walter, F., et al. 2011, AJ, 142, 37
Smith, J. D. T., Draine, B. T., Dale, D. A., et al. 2007, ApJ, 656, 770
Sutter, J., & Fadda, D. 2022, ApJ, 926, 82
Tielens, A. G. G. M. 2008a, ARA&A, 46, 289
Tielens, A. G. G. M. 2008b, ARA&A, 46, 289
Walter, F., Brinks, E., de Blok, W. J. G., et al. 2008, AJ, 136, 2563
Weingartner, J. C., & Draine, B. T. 2001, ApJS, 134, 263
Wolfire, M. G., Hollenbach, D., McKee, C. F., Tielens, A. G. G. M., & Bakes, E. L. O. 1995, ApJ, 443, 152
Wong, T., Xue, R., Bolatto, A. D., et al. 2013, ApJL, 777, L4